A 260 megapixel visible/NIR mixed technology focal plane for space

Robert W. Besuner[1], Christopher J. Bebek[2], Gunther M. Haller[3], Stewart E. Harris[1], Philip A. Hart[3], Henry D. Heetderks[1], Patrick N. Jelinsky[1], Michael L. Lampton[1], Michael E. Levi[2], Sergio E. Maldonado[3], Natalie A. Roe[2], Aaron Roodman[3], Leonid Sapozhnikov[3]

[1] U.C. Berkeley Space Sciences Laboratory
[2]Lawrence Berkeley National Laboratory
[3]SLAC National Accelerator Laboratory

ABSTRACT

Mission concepts for NASA's Wide Field Infrared Survey Telescope (WFIRST)[1,2], ESA's Euclid[3,4] mission, as well as next-generation ground-based surveys require large mosaic focal planes sensitive in both visible and near infrared (NIR) wavelengths. We have developed space-qualified detectors, readout electronics and focal plane design techniques that can be used to intermingle CCDs and NIR detectors on a single, silicon carbide (SiC) cold plate. This enables optimized, wideband observing strategies. The CCDs, developed at Lawrence Berkeley National Laboratory, are fully-depleted, p-channel devices that are backside illuminated and capable of operating at temperatures down to 120K. The NIR detectors are 1.7 μm and 2.0 μm wavelength cutoff H2RG® HgCdTe, manufactured by Teledyne Imaging Sensors under contract to LBNL. Both the CCDs and NIR detectors are packaged on 4-side abuttable SiC pedestals with a common mounting footprint supporting a 44 mm mosaic pitch. Both types of detectors have direct-attached readout electronics that convert the detector signal directly to serial, digital data streams and allow a flexible, low cost data acquisition strategy to enable large data rates. A mosaic of these detectors can be operated at a common temperature that achieves the required dark current and read noise performance necessary for dark energy observations. We report here the qualification testing and performance verification for a focal plane that accommodates a 4x8 array of CCDs and HgCdTe detectors.

Keywords: JDEM, WFIRST, CCD, HgCdTe, Silicon Carbide, Space Telescope

1 INTRODUCTION

Large, multi-detector mosaic telescope focal planes along with advances in wide-field telescope optics[5] are enabling technologies for the next generation of large area astronomical surveys from space, such as the proposed WFIRST and Euclid space telescopes. Mixed-technology focal planes with both visible and near infrared (NIR) detectors[6] open even more surveying possibilities including photometric redshift measurements as envisioned in the proposed NASA/Department of Energy Joint Dark Energy Mission (JDEM) space telescope[7].

We have developed technology to construct mixed-technology focal planes suitable for space and ground applications, and have implemented this technology on a 4x8 detector technology demonstrator, shown in Figure 1 and Figure 2. The focal plane technology has been developed in parallel with and complementary to CCD[8,9,10] and NIR detector[11] packaging, which have separately been tested and verified. The performance of the technology demonstrator has been verified by successful functional, vibration, thermal, radiation, and metrology testing.

Infrared Sensors, Devices, and Applications; and Single Photon Imaging II, edited by Paul D. LeVan, Ashok K. Sood, Priyalal S. Wijewarnasuriya, Manijeh Razeghi, Jose Luis Pau Vizcaíno, Rengarajan Sudharsanan, Melville P. Ulmer, Tariq Manzur, Proc. of SPIE Vol. 8155, 81550D · © 2011 SPIE · CCC code: 0277-786X/11/$18 · doi: 10.1117/12.893777

Figure 1: 4x8 Cold Plate in handling fixture, with 16 CCDs and 16 NIR detectors

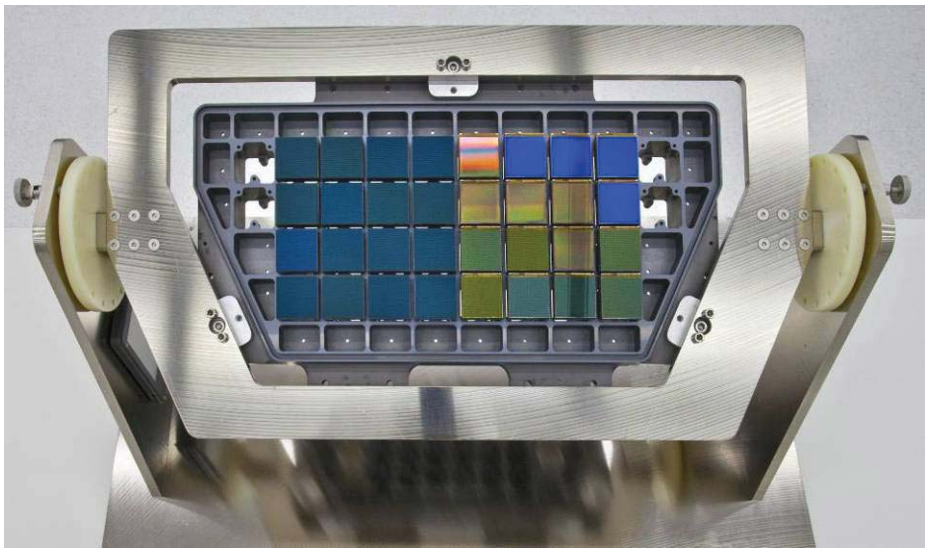

Figure 2: 4x4 array of LBNL CCDs installed to the left, 4x4 array of Teledyne H2RG® NIR detectors located to the right. Additional detector mount positions for guiding detectors and calibration phodiodes are outboard of the 4x8 array. Detector pitch is 44.1 mm.

2 PERFORMANCE GOALS

Performance goals for this technology demonstrator are based on requirements established for the former proposed SuperNova/Acceleration Probe[12] (SNAP) and JDEM space telescopes. These stringent requirements for space applications make this technology suitable for other space missions as well as for ground-based applications.

Some of the key mechanical and thermal performance goals include:
-Survival of launch and service environments per NASA's GEVS specifications[13]
-Detector focal surface flatness better than 40 µm P-V cold
-Operating at temperatures as low as 120K
-Accommodating a front-end electronics (FEE) module that fits within the detector footprint
-Rejecting heat through conduction to peripheral thermal straps
-Maintaining temperature uniformity across the focal plane better than 5K.

Some key functional goals include:
-Synchronous operation of CCD and NIR to minimize opportunity for crosstalk between detectors
-Common clock for both types of detectors, as a result of the first goal
-Simultaneous readout of all detectors
-Common exposure time for both types of detectors
-Total noise for 1.7 µm H2RG less than 7 electrons (e^-) rms for Fowler-16
-Read noise for CCDs less than 4 e^-.

3 DESIGN OF TECHNOLOGY DEMONSTRATOR

Figure 3 illustrates the overall mechanical layout of the 4x8 technology demonstrator. The main structural element of the demonstrator is the silicon carbide (SiC) cold plate, shown in Figure 4. The mechanical and thermal properties of SiC make it an excellent material for the cold plate, as well as for the detector bases. It has fairly low mass density, high strength, high modulus of elasticity, high thermal conductivity, and a CTE which is a good match to that of silicon. The surface of the cold plate to which the detectors mount is ground flat to within 2 µm P-V. The detectors and their associated FEE modules fasten directly to the cold plate using thermally-compensated titanium screws.

The cold plate is supported on three titanium bipods with crossed flexure pairs at the end of each leg to minimize focal plane distortions due to displacements or misalignments of the mounting feet and to provide thermal resistance between

the telescope and the focal plane. These bipods are fastened to Invar inserts that are bonded to the cold plate. The aluminum front aperture mask and rear enclosure each mount to those same Invar inserts via three titanium blade flexures, to minimize their influence on the cold plate flatness. To maintain light-tightness, the mask and enclosure employ non-contacting labyrinth seals around their peripheries where they meet the cold plate.

Four printed circuit boards, known as quadrant boards, fasten to the inside walls of the rear enclosure. As shown in Figure 5, one flex circuit is connected to the rear end of each FEE and to its nearest quadrant board. The quadrant boards bring the signal and power connections outside the rear enclosure via connectors that penetrate the rear enclosure's walls. An aluminum rear cover completes the assembly. The total mass of the assembly is 21.9 kg.

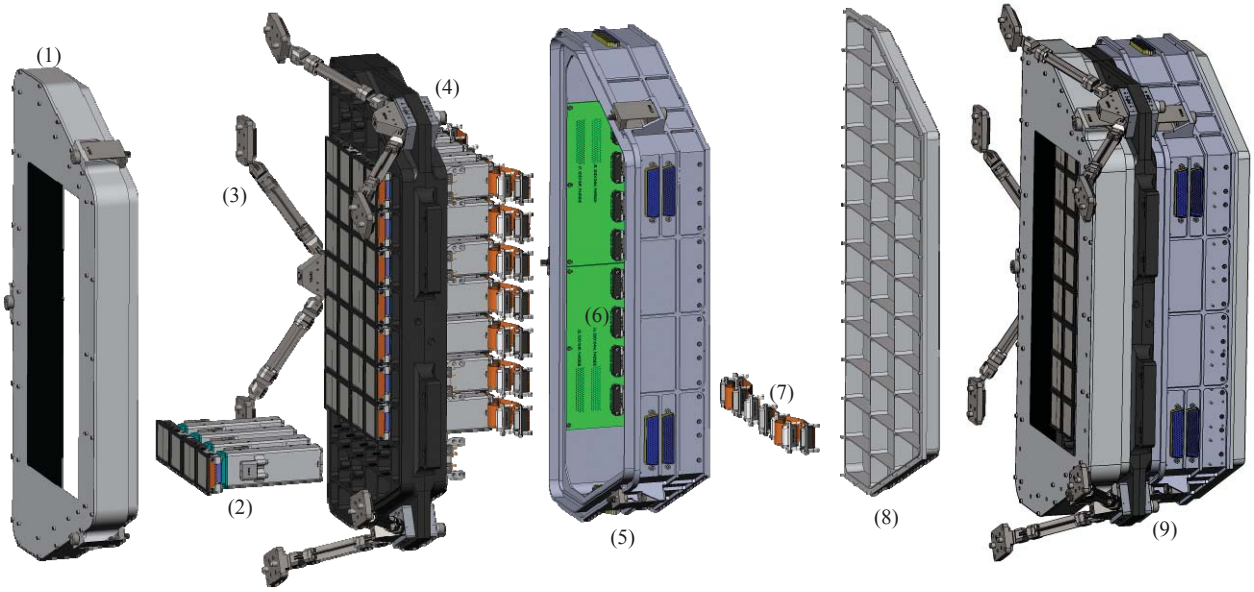

Figure 3: 4x8 demonstrator assembly: (1) Aluminum aperture mask with labyrinth light seal to cold plate, mounts to cold plate inserts on 3 Ti flexures. (2) Four detectors/FEEs to be installed to cold plate. (3) Ti bipods with crossed-flexure ends. (4) SiC cold plate with 28 detectors/FEEs installed. (5) Aluminum rear enclosure, with labyrinth light seal to cold plate, mounts to cold plate inserts on 3 Ti flexures. (6) Quadrant board mounted to rear enclosure. (7) Flex circuits from FEEs to quadrant boards. (8) Rear cover. (9) Complete assembly.

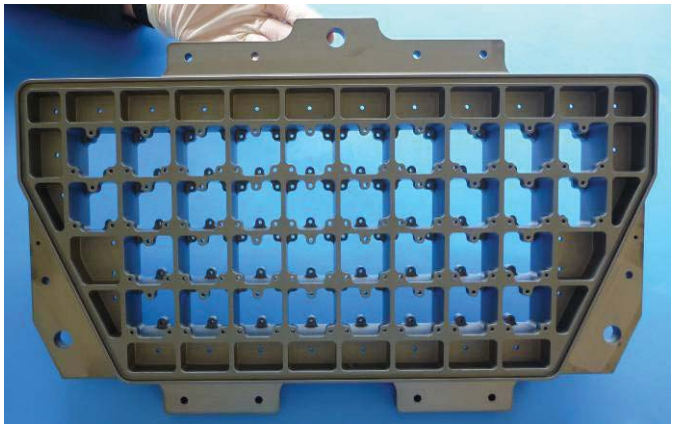

Figure 4: SiC cold plate, prior to bonding of bipod mount inserts. The smaller holes on ears around the periphery are mounting features for flexible thermal straps to carry heat to a radiator. Material is UltraSiC from Coorstek.

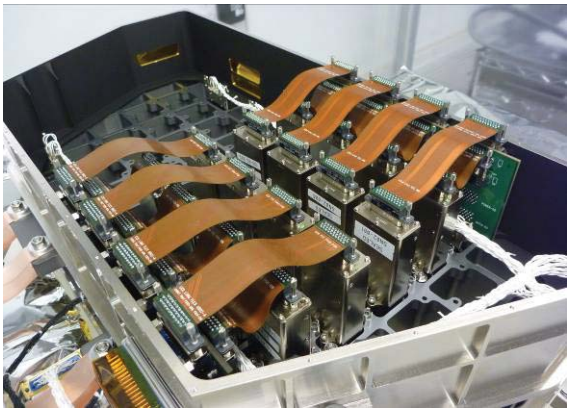

Figure 5: View inside the half-populated rear enclosure, showing FEEs, flex circuits, and quadrant boards

4 DETECTORS/ELECTRONICS

Figure 6 illustrates the electronic architecture of the demonstrator. Photons enter the detectors, generating analog signals that feed into the FEE modules, immediately behind the detectors on the cold plate. The FEEs digitize the data, which then pass through flex circuits to the quadrant boards. Each quadrant board funnels signals and power from eight FEEs to a single signal connector and a single data connector. Flex harnesses connect the four quadrant boards to the warm electronics modules that provide science data collection, power, control, and monitoring functions.

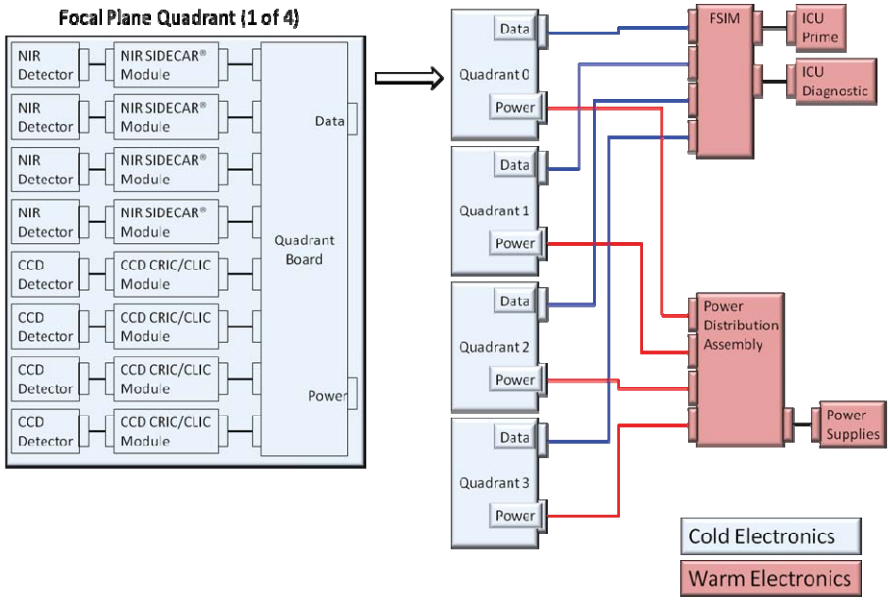

Figure 6: Electronic architecture of the 4x8 technology demonstrator.

The visible detectors employed in the mixed-technology focal plane are 3.5k x 3.5k, 10.5 µm CCDs developed and packaged at Lawrence Berkeley National Laboratory (LBNL)[14,15], and the NIR detectors are 2k x 2k, 18 µm Teledyne Imaging Systems (TIS) H2RG® HgCdTe detectors employing LBNL-developed packaging. The packaging for both types of detector and their front end electronics modules (FEE) allows either type to be mounted in the same way at any position on the focal plane. After packaging and preliminary metrology, precision spacers are mounted to each detector to ensure the best-fit plane of the optical surfaces of all the detectors, of both types, are 15.000±0.0015 mm above their mounting surfaces. This ensures all the detector surfaces will be placed coplanar within the tolerance required by telescope optics. Both detector technologies function well in the temperature range 120K-140K.

Figure 7. Back-illuminated SNAP/JDEM CCD mounted on flight configuration 4 side abuttable SiC pedestal. The format is 3.5k × 3.5k, 10.5 µm pixels with four corner readout. The CCD is 200 µm thick for extended red response.

Figure 8 2k × 2k, 18 µm pixels, 1.7 µm cutoff HgCdTe NIR detector hybridized and mounted on SNAP/JDEM custom, flight configuration, 4 side abuttable, SiC pedestal.

Figure 9. Top, 32-channel NIR detector readout module with TIS SIDECAR® ASIC. The right connector mates to the detector. Bottom, CRIC-CLIC ASIC module for a CCD. The connector on the right mates to the CCD detector module.

4.1 LBNL CCDs

An enabling technology for the focal plane is the fully-depleted, high-resistivity, p-channel CCD developed at LBNL Micro Systems Lab.[16,17,18,19,20,21] Full-depletion provides enhanced quantum efficiency out to one micron,[22,23,24] and the p-channel architecture has superior radiation tolerance.[25,26,27] The CCD is designed to operate with an over-depleted substrate bias to reduce the lateral charge diffusion,[28,29,30] a contributor to the overall point spread function (PSF). Photodiodes fabricated at LBNL, using the same full-depletion technology featured on the LBNL CCDs are currently operating in space on the THEMIS mission[31]. The SNAP/JDEM CCDs (see Figure 7) are packaged with a silicon carbide (SiC) base for dimensional stability, high thermal conductivity, and compatibility with the demonstrator cold plate. Each CCD module has a mass of 58 grams.

4.2 Teledyne H2RGs

The NIR detectors utilize HgCdTe hybridized to the H2RG® readout integrated circuit by TIS. TIS devices have been successfully deployed in space programs, HST SM5 and WISE, and will be used on JWST. For SNAP/JDEM, in addition to the science detectors, two to four of these detectors would serve as through-the-telescope tracking detectors for fine guidance and pointing. SNAP/JDEM H2RGs® with cutoff wavelengths of both 1.7 μm and 1.95 μm are produced on LBNL-designed SiC bases (see Figure 8), with mounting features identical to those of the SNAP/JDEM CCDs. Extensive testing and characterization of these detectors has been done by SNAP/JDEM collaborators at the University of Michigan and Caltech[32,33,34,11]. Each NIR detector module's mass is 66 grams.

4.3 Front End Electronics Modules

An essential aspect of the 4x8 focal plane electrical architecture is the implementation of a photon-to-bits paradigm in which the detectors and readout electronics are co-located on the focal plane cold plate. The FEE modules are mounted directly behind each detector, and are thermally connected to the SiC cold plate, conducting most of their generated heat directly to the cold plate via conductive flexures, and operating at a temperature very close to the detectors themselves. The FEEs may be blind-mated and de-mated with installed detectors or they may be installed pre-mated with the detectors. The FEE provide all the required bias voltages, clock signals and signal processing electronics required such that only digital data is transferred between the FEE and the data acquisition system that operates at room temperature. The mass of each front end electronics module is approximately 101 grams.

The NIR front-end electronics (Figure 9, top) utilizes the TIS SIDECAR® ASIC, which provides all the biases and clocks required to operate the Hawaii-2RG® family of devices. Approximately 2,000 lines of application-specific microcode, developed at TIS and SLAC, are loaded into the SIDECAR® ASIC. This software enables 32-channel readout mode with outputs to 4 serial channels, along with processing serial commands and monitoring and managing resources. In radiation testing up to 80 krad (Si) with 63 MeV protons, these devices showed no performance degradation or single event upsets (SEUs). The NIR detectors are read out at 100 kHz, with a 16-bit ADC. Power dissipation for the NIR front end electronics is 300 mW continuous per module.

The control and signal digitization of the CCD detectors is accomplished with a pair of ASICs. The CRIC ASIC performs detector signal analog processing and digitizing.[35,36,37,38] The CLIC ASIC provides voltage biases, clock level generation, and clock pattern sequencing.[39] The CCDs are read out at 100 kHz, with a 14-bit ADC with three digitization ranges. Both ASICs have been extensively tested cryogenically and for total ionizing dose and heavy ion radiation effects. The ASICs are mechanically packaged in an enclosure identical to that of the NIR FEEs (Figure 9, bottom). Average power per module is 500 mW.

4.4 Warm Electronics

Image data from the FEEs are transferred serially to the focal plane signal interface module (FSIM) where single images from the detectors are pre-processed and buffered. For NIR detectors, the FSIM can acquire single images, Fowler images (up to Fowler-64) and up-the-ramp and multi-accumulate images. The FSIM synchronizes commands and data to all the detectors.

Overall control of the instrument is managed by the instrument control unit (ICU), which is based on cPCI architecture using the GE Fanuc PowerPC750 processor. The ICU is dedicated to science data compression, FSIM command and control, housekeeping, exposure sequencing, and monitoring. It accepts commands from the Electrical Ground Support Equipment (EGSE) PC and sends them to the FSIM. It also buffers the data from the FSIM before sending to the EGSE

PC. It has heritage from the FERMI (formerly GLAST) Gamma-ray space telescope[40]. All communication between ICU, FSIM and the FEEs uses 25 MHz serial communication links based on, and compatible with, the Teledyne SIDECAR® serial communication protocol.

5 TESTING/PERFORMANCE

We have performed rigorous functional, thermal, vibration, radiation and flatness testing on the detectors and electronics as components and on the focal plane as a system. We believe the successful completion of these tests (to NASA GEVS qualification levels, where applicable) demonstrates these technologies are at NASA Technical Readiness Level 6 (TRL 6), meaning "System/subsystem model or prototype demonstration in a relevant environment." [41]

5.1 Electrical testing

5.1.1 Test Criteria

The simultaneous operation of all CCDs and NIR detectors imposes some unique requirements on the timing of image readout. To minimize the opportunity for crosstalk, the system was designed to keep data readout as synchronous as possible. For this reason, the detectors are operated on a common, master reference frequency. All CCDs are exactly synchronous, with pixel shifts in both the vertical and horizontal direction timed the same,. All NIR detectors are similarly synchronous, with pixel reads and multiplexer switching occurring simultaneously. However, due to the very different nature of CCD and NIR readout, the level of synchronization possible between the NIR and CCD is limited to beginning readout at the same time and having exposure times very nearly the same.

For the 4x8 focal plane, the FSIM synchronizes readout to coincide with the basic frame readout period of the NIR detectors. To maintain the H2RG® detectors in a thermally stable state, they are continuously reading pixels, but only sending frames of data to the FSIM, when needed. This cadence of NIR frame readout has a period of ~1.5 seconds, and it is controlled by the FSIM, which is programmed to send commands to the NIR at this rate. The readout of the CCDs is therefore also timed to this cadence, with CCD readout commanded to begin at the same time NIR readout begins. Depending on the operating mode of the NIR, many more frames of data may transfer from the NIR than will transfer from the CCDs.

Within this operating environment, we require that each detector meets the performance requirements, as described in Section 2, for either an imaging or spectroscopic dark energy mission application.

5.1.2 Functional testing

The verification of electrical functional requirements has taken place in successively larger mosaics of mixed focal plane assemblies. Initially we started with a 2x2 configuration of 2 CCDs and 2 NIR detectors mounted on a SiC cold plate that was sized to accommodate a 3x3 configuration. Then a 4x8 SiC cold plate was fabricated, and we have taken the same step-wise approach to populating and testing this focal plane. At first, we populated one quadrant, a 2x4 array of 4 CCDs and 4 NIR. More recently we have moved to a 4x4 array, with 8 CCDs and 8 NIR. Functional and performance testing was done at each stage.

Throughout this testing, we have been concerned about the potential for crosstalk between detectors. During the initial testing of the 2x2 array, an LED illuminator and mask were used to create sharply focused images that could be used to explore this possibility. For the CCDs visible LEDs (570 nm) were used, and IR LEDs (1500 nm) were used to illuminate the NIR detectors. A resulting image is shown in Figure 10. Even with very high intensity lighting, saturating the detectors by 10X, or more, on either the CCDs or NIR detectors, no detectable artifacts could be seen in neighboring detectors, or in adjacent channels of the same detectors.

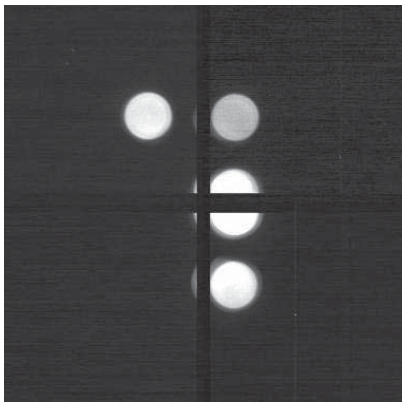

Figure 10. A CCD image of LED illuminated spots. This is the central 1800x1800 pixels of the CCD array. The dark bands in the middle, separating the quadrants, are the CCD overscan, which is included in each readout.

As larger arrays of detectors have been tested, we have continued to look for occurrence of crosstalk, or degraded noise performance in the detectors, that may result from crosstalk. In general we've found no evidence of degraded performance as a result of having multiple detectors operating on a single focal plane. This is a testament to the photon-to-bits paradigm, that works exceedingly well in keeping the sensitive analog outputs of the detectors as close to the signal processing electronics as possible, and producing good data despite the multitude of detectors operating nearby. The one exception to this has only recently occurred, when we moved from the 2x4 to the 4x4 configuration. It was at this stage in the development that we finally saw evidence of interference between detectors.

In Figure 11 we see the observed crosstalk. In this case the detectors receiving the interference were the 4 NIR detectors located in the middle of the array as seen in Figure 12. The location of these 4 NIR is different than the upper row of NIR, in that they are located between two rows of CCDs, a situation that was not encountered until two quadrants of detectors had been populated. This clue, and other tests we performed, convinced us that the coupling of the interference was occurring on the focal plane. From Fourier analysis of the noise bursts in the NIR images, we also found that their frequency of occurrence was about 50 Hz, the same frequency as the CCD parallel transfer rate. With this knowledge, we speculated that the point of coupling was located directly at the outputs of the H2RG® detectors, which are connected to the FEE via a flex circuit that provides no shielding. Because of the geometry of the focal plane, only those 4 NIR detectors are located such that the flex circuit passes next to a CCD. We tested this theory by placing a grounded EMI shield between those NIR and the neighboring CCDs. This simple shielding eliminated the crosstalk, as seen in Figure 11, and suggests that the NIR flex circuits should include additional shielding.

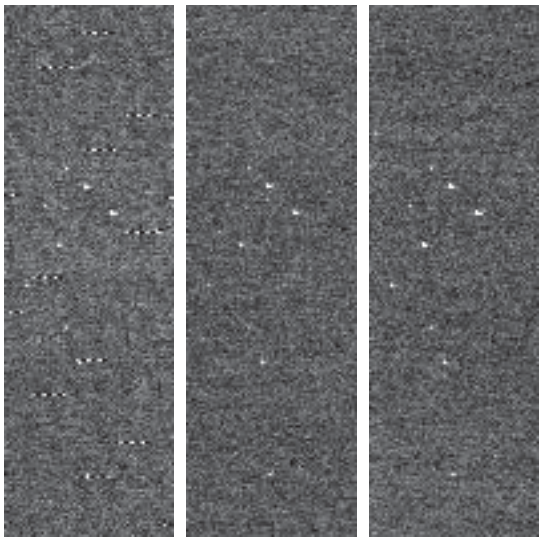

Figure 11: Example of crosstalk on one of the Quadrant 2 NIR detectors caused by CCD parallel clocking. Left panel shows interference occurring with the CCDs operating. Middle panel is the same detector with CCDs not operating. Right panel is the same detector with CCDs operating, but with an EMI shield inserted next to the NIR flex circuit. These image snippets are taken from an average of 50 Fowler-1 difference images. In single difference frames, the interference was lost in the noise.

Figure 12: Photo of two quadrants populated on the focal plane. CCDs and NIR detector rows alternate, with NIR on the top row, followed by CCD row, and so on. The detectors in the third row down are NIR detectors and were susceptible to parallel clock interference from the CCDs just above them, while the top row of NIR were not. Note that the NIR wire bonds and flex circuit are adjacent to a row of CCDs. This was the likely area where noise was coupling into the H2RG® outputs, and was easily shielded.

5.1.3 Performance testing

To verify that detectors were achieving the specified noise performance, it was necessary to verify that the conversion gain of the detectors and readout electronics were at the expected level. We measured the conversion gain using the photon transfer method[42]. This required a well controlled light source for the focal plane, which was implemented by equipping the front closeout of the focal plane with LEDs that would provide nearly uniform illumination for detectors in one quadrant (the lower two rows in Figure 12). The LEDs, both visible (570 nm) and infrared (1500 nm), are pulsed at 1 μs or 0.1 μs duration, at a repetition rate of 10 kHz. In this manner, very repeatable exposures could be integrated on either the CCDs or NIR detectors, and varied by controlling the number of pulses. With this illumination system a series of exposures were taken at increasing light levels, and the variance vs. mean signal was quantified.

For the CCDs, the procedure is made somewhat simpler in that only two images at each exposure level are needed to adequately measure the noise in the illuminated images. For the NIR, however, we found that the spatially sampled data, as used for CCD analysis, is not adequate to accurately characterize the detectors. So NIR exposure acquisitions required many more samples at each exposure level, so that a reasonably long time series of data could be acquired for each pixel in the detector. For our tests, we used 50 exposures, at each exposure level.

Figure 13 and Figure 14 show the results for one CCD in the focal plane. With four quadrant readout, 100 kHz serial clock rate, the LBNL CCDs demonstrate less than 4 e^- noise rms in each quadrant. This performance was demonstrated on four of the eight CCDs, with all 16 detectors being readout simultaneously. This was the expected result, since not all the devices used in the testing are science grade.

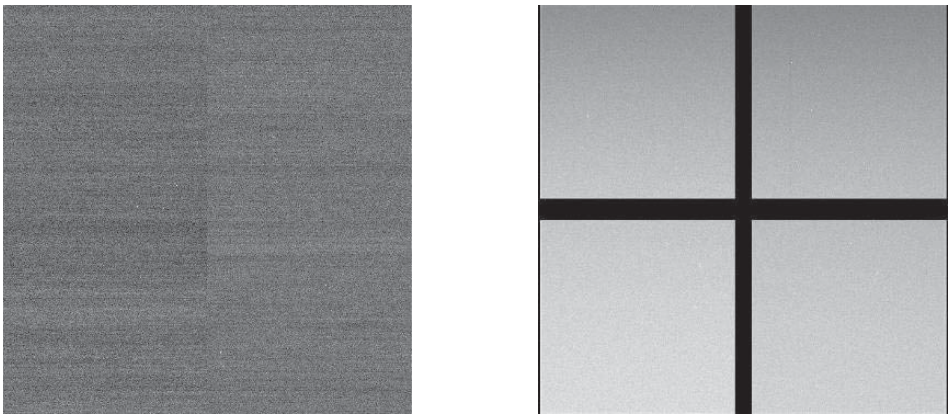

Figure 13: The image on left is a bias image from one CCD (#34) on the focal plane. The image to the right is illuminated with visible LED light, pulsed 100 times. The dark cross in the middle of the image is the overscan readout from the CCD.

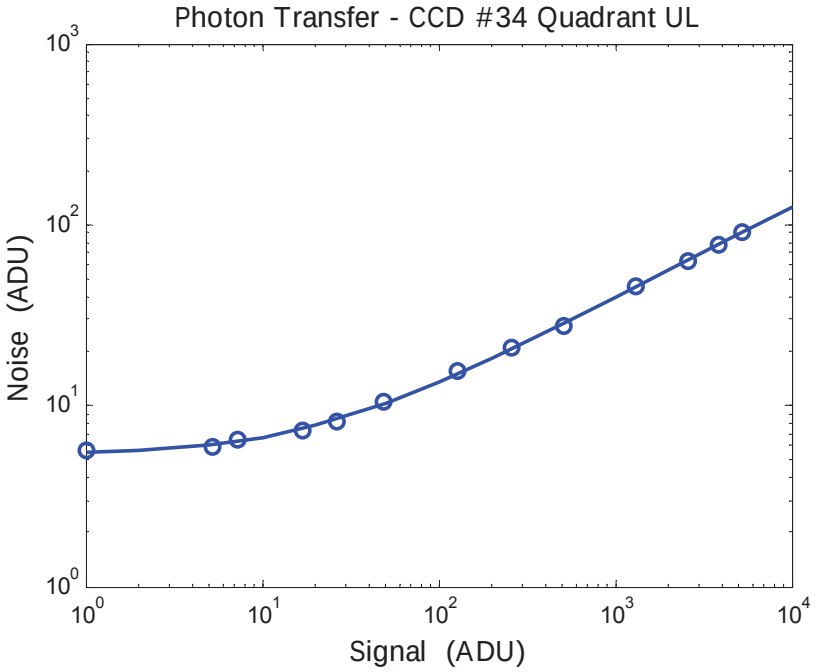

Figure 14: Photon transfer curve for one quadrant of the detector of Figure 13. The data indicate a conversion gain of 0.65 e-/ADU and read noise of 3.7 e- rms.

Figure 15 shows the results for one H2RG® detector, with 1.7 µm wavelength cutoff. The image is the Fowler-1 read noise converted to electrons using gain values computed for each pixel from photon transfer statistics. The faint image artifact in the lower left hand corner is an indication that some adjustment of bias levels is still required for this detector. Nonetheless the noise performance is within family for these detectors. All image data acquisition was done with all NIR and CCD detectors reading out simultaneously. Figure 16 is the similar data from a detector with 1.95 µm wavelength cutoff. For this detector, we operated the focal plane at a lower temperature, 120K.

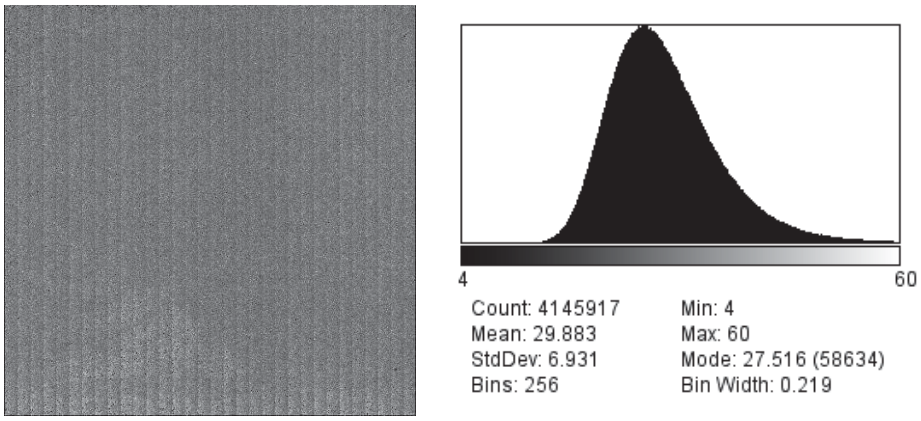

Figure 15: Image on left is the Fowler-1 noise map for NIR #16072, a detector with 1.7 μm cutoff, operating at 135K. The histogram on right shows a peak at 27.5 e- noise, which is typical for these detectors, and achieves ~7 e- noise with Fowler-16.

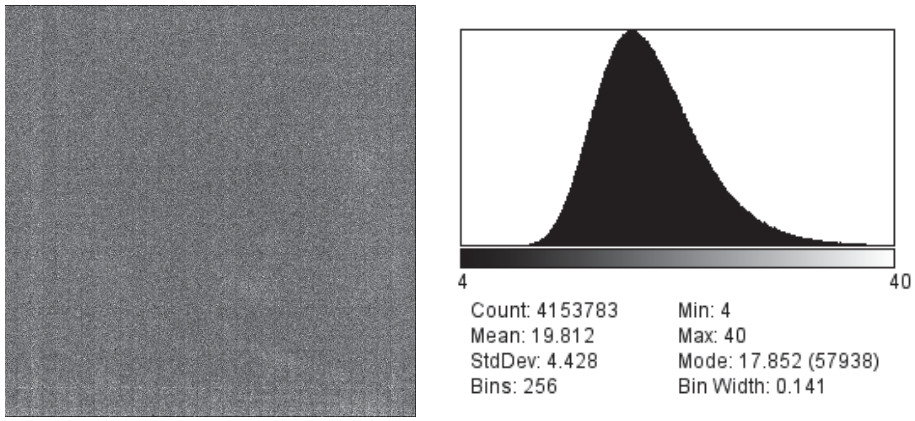

Figure 16: Image on left is the Fowler-1 noise map for NIR #16071, a detector with 1.95 μm cutoff, operating at 120K. The histogram on right shows a peak at 17.9 e- noise. This is significantly lower than the 1.7 μm devices on the focal plane.

The experience that we've now had with large mosaics of detectors provides a good demonstration that the performance of individual detectors can be as good when operating in concert with many detectors, as it is when operating alone. This is a welcome result, and one that can inform designers for upcoming space missions. We think the critical design aspect responsible for this result is the front end electronics co-located on the focal plane, as close as possible to the detectors. This configuration provides the best immunity to noise and crosstalk. The results provide confidence that detectors can be characterized in a standalone configuration, and their performance will not change when the detectors are integrated into a larger system.

5.2 Vibration testing

Vibration testing was performed at the component level and the system level as proscribed in NASA's GEVS specification. Figure 17 and Figure 18 show the configuration used for component-level vibration tests of the detector/FEE elements. In these tests, a working detector was mated with a working FEE in an aluminum fixture with mounting features identical to the full cold plate. The fixturing featured acrylic windows to provide contamination protection and allow visible inspection at the vibration facility. In addition, it included access holes to measure the locations of the detector and FEE before and after vibration to determine if any joint slippage occurred. The detector/FEE pair were vibrated to the full GEVS random 14.1 G_{rms} qualification level in three axes, and no damage, slippage, or sine-sweep signature change was noted. Functional testing before and after vibration showed no damage or change in characteristics.

Figure 19 shows the complete 4x8 system on a vibration slip plate for the system-level vibration test. Because the detectors and FEEs were tested at the component level, and to minimize contamination and electrostatic discharge

protection requirements, the full system vibration test was conducted with mass dummy representations of the detectors and FEEs. Surrogate flex circuits and representative thermal straps extend from the demonstrator to fixed locations on the vibration adapter plate. The mass of the article under test was 21.9 kg. Tests performed in three axes included random vibration to notched GEVS 14.1 G_{rms} qualification levels and sine-burst tests at amplitudes of 33 g (1.25 times design limit load of 26.2 g) and frequencies of 50 Hz. All components survived without visible damage, loss of function, or sine signature shift.

Figure 17: FEE extending from single-detector/FEE vibration fixture for component-level test

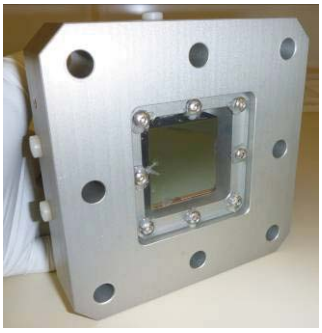

Figure 18: Single NIR detector in single-detector/FEE vibration fixture for component-level test

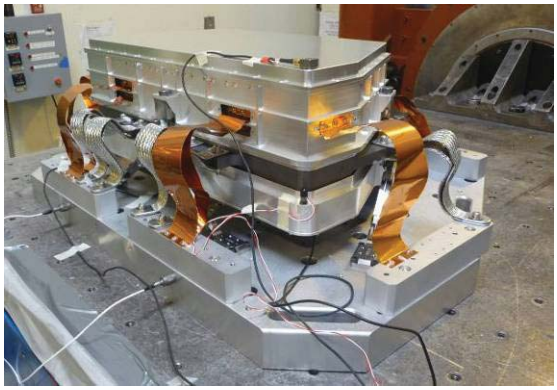

Figure 19: 4x8 demonstrator on shaker slip plate

5.3 Radiation Testing

The LBNL CCD, CRIC/CLIC, SIDECAR® and H2RG® have all been radiation tested. The LBNL CCD has been tested with protons of 12.5 and 55 MeV up to a dose of $1x10^{11}$ protons/cm^2 and electrons from 0.1 to 1 MeV at 1.2 krad[43]. The LBNL CCD was ~10 times more radiation tolerant than the CCDs used on the HST ACS instrument. They easily meet the end of life (EOL) requirements for a 5 year mission in orbit around the L2 Earth-Sun libration point. Post-radiation charge transfer efficiency measurements have been used in a shape distortion simulation that shows that the stringent PSF requirements of a weak lensing survey can be met[44]. The CRIC was tested with an ion beam at 4.5 MeV/nucleon and shown to meet the EOL requirements for a 5 year L2 mission[37]. The CLIC has also undergone single event upset (SEU) radiation testing and meets the EOL requirements[45]. The SIDECAR® has been tested up to 80 krad (Si) with 63 MeV protons, these devices showed no performance degradation or SEUs[46]. The H2RG® has undergone radiation testing and is at a TRL 6 readiness level[47].

5.4 Thermal Testing

A thermal vacuum chamber (door visible in background of Figure 1) for testing the technology demonstrator was installed at the focal plane assembly clean room. This chamber includes feedthroughs for all the demonstrator harnesses, along with temperature monitors and liquid nitrogen for cooling. In addition it includes features to enable use of flatness measurement equipment, allow installation of a moveable Fe^{55} radiation source (for detector gain measurements), and to install a flat field illumination system. All functional, thermal, and flatness testing of the demonstrator was performed in this chamber.

Figure 20: 4x8 demonstrator being prepared for thermal vacuum testing. Cold finger and thermal straps visible to the left.

Figure 21: 4x8 demonstrator blanketed in MLI, installed in thermal vacuum chamber. Flex harnesses visible in lower left.

For testing in the vacuum chamber, the 4x8 demonstrator is mounted on its bipods to an adapter plate, which is supported on three titanium blade flexures in the chamber (see Figure 20 and Figure 21). Two cold fingers with liquid nitrogen plumbed through them are also mounted on thermal isolators to the adapter plate. The cold fingers are thermally linked to the cold plate thermal ears using thin copper straps. The demonstrator and cold fingers are wrapped in multilayer insulation (MLI) to minimize thermal radiation coupling with the warm adapter plate and chamber walls. Heaters and temperature monitors on the cold plate are used for fine temperature control of the demonstrator.

Testing included operating detectors and FEEs during thermal excursions as low as 120K and numerous excursions down to 135K. No physical damage or mechanical changes have been noted after numerous thermal cycles. Thermal gradients across the cold plate were found to be 2K or less during all cold operational modes, beating the performance goal of 5K or less.

5.5 Cold Flatness Testing

The door of the thermal vacuum chamber described in section 5.4 includes features to which the novel Local Zone Slope (LZS) focal plane flatness measurement system is mounted[48]. This optical system tracks changes in slope of the detector and cold plate surfaces as the demonstrator is cooled. Deviations of flatness from the room-temperature configuration can then be inferred and the net flatness of the entire focal surface at operating temperatures determined. Recent and preliminary results indicate deflections over the entire surface of the cold plate less than 5 μm. CCD and NIR detector room temperature flatness measurements have shown them all to be better than 10 μm P-V. Flatness changes of the detector surfaces due to cooling are less than 1 μm for NIR detectors and less than 8 μm for CCDs. Direct summing of the contributors to flatness deviation (including 3 μm P-V for detector height tolerance) gives a maximum deviation from flat of 26 μm P-V, much better than the design goal of 40 μm P-V.

6 CONCLUSION

We have developed detector, readout electronics, and focal plane technologies that allow high-performance, astronomy-grade visible and NIR detectors to be co-located on a single focal plane. We have constructed a technology demonstrator with a 4x8 detector array to verify the performance of this technology. Functional testing demonstrates that the detectors can operate without crosstalk or interference with each other. Environmental testing shows that the technology meets NASA Technical Readiness Level 6 and is qualified for space missions.

This scalable technology has been shown by analysis to be suitable up to at least a 76-detector configuration, and likely could be scaled even larger. The technology is adaptable to ground-based applications as well as space-borne missions and enables very wide astronomical surveys from 350 nm to 2 μm.

ACKNOWLEDGMENT

This work was supported by the Director, Office of Science, of the U.S. Department of Energy under Contract No. DE-AC02-05CH11231.

REFERENCES

[1] Levi, M., et al., "Science Yield of an improved Wide Field Infrared Survey Telescope (WFIRST)," arXiv 1105.0959 (2011).
[2] Sholl, M., et al., "A Practical Implementation of the Wide Field InfraRed Survey Telescope WFIRST," 217th AAS, Seattle, 433.04 (2011).
[3] Wallner, O., et al., "Euclid Mission Design," Proc. Intl. Conf. Space Optics ICSO 2010, Rhodes Greece (2010).
[4] Duvet, L., "Euclid Reference Payload Concept," SRE-PA /2010.030, European Space Agency, ftp://ftp.rssd.esa.int/pub/EUCLID-ITT/documents (2010).
[5] Sholl, M., et al., "Widefield spectroscopy and imaging at two plate scales with a focal three mirror anastigmat," Proc. SPIE 7731, 77311F (2010).
[6] Jelinsky, P., et al., "The design and integration of multiple technology focal planes," American Astronomical Society 217th Meeting, Seattle, 433.02 (2011).
[7] Sholl, M., et al, "Observatory Conceptual Development for the Joint Dark Energy Mission," Proc. SPIE 7436, 743603 (2009).
[8] Bebek, C., et al., "Fully depleted back-illuminated p-channel CCD development," Proc. SPIE 5167, 50 (2004).
[9] Baltay, C., et al., "Space qualified abuttable packaging for LBNL p-channel CCDs, Part I," Proc. SPIE 7742. 77422E (2010).
[10] Besuner, R., et al., "Space qualified abuttable packaging for LBNL p-channel CCDs, Part II," Proc. SPIE 7742, 77420H (2010).
[11] Shubnell, M., et al, "Near Infrared Detectors for SNAP," Proc. SPIE 6276, 62760Q (2006).
[12] Aldering, G., et al., "Overview of the SuperNova/Acceleration Probe (SNAP)," Proc. SPIE 4835, 146-157 (2002).
[13] General Environmental Verification Standard (GEVS), NASA Publication GSFC-STD-7000, April 2005.
[14] Holland, S., et al., "Device Design for a 12.3-Megapixel Fully Depleted Back-Illuminated High-Voltage Compatible Charge-Coupled Device," IEEE Trans. Electron Devices 56, 2612-2622 (2009).
[15] Roe, N., et al., "Radiation-tolerant, red-sensitive CCDs for dark energy investigations," Nucl. Instrum. Methods A 572, 526-527 (2007).
[16] Holland, S., et al., "High-voltage-compatible, fully depleted CCDs," Proc. SPIE 6276, 67260B (2006).
[17] Kolbe, W., et al., "CCD Development Progress at Lawrence Berkeley National Laboratory," Scientific Detectors for Astronomy 2005, J. E. Beletic, J. W. Beletic, P. Amico editors, Springer (2006).
[18] Bebek, C., et al., "Development of Fully Depleted, Back-Illuminated Charge Coupled Devices," SPIE 5499, 140 (2004).
[19] http://www-ccd.lbl.gov/.
[20] Stover, R., et al., "Characterization of a fully depleted CCD on high resistivity silicon," Proc. SPIE 3019, 183 (1997).
[21] Stover, R., et al., "High performance CCD on high resistivity silicon," Proc. SPIE 3505, 13 (1998).
[22] Groom, D., et al., "Quantum efficiency of a back illuminated CCD imager: an optical approach," Proc. SPIE 3649, 80 (1999).
[23] Groom, D., et al., "Quantum efficiency characterization of LBNL CCDs: Part I. The quantum efficiency machine," Proc. SPIE 6068, 60680F (2006).
[24] Fabricius, M., et al., "Quantum efficiency characterization of back-illuminated CCDs: Part II. Reflectivity measurements," Proc. SPIE 6068, 60680G (2006).
[25] Bebek, C., et al., "Proton Radiation Damage in P-Channel CCDs Fabricated on High-Resistivity Silicon," IEEE Trans Nucl. Sci. 49 (2002).
[26] Bebek, C., et al., "Proton radiation damage in high-resistivity n-type silicon CCDs," Proc. SPIE 4669, 161 (2003).
[27] Dawson, K., et al., Radiation Tolerance of High-Resistivity LBNL CCDs, IEEE NSS, N09-6, 2006.

[28] Groom, D., et al., “Point-spread function in depleted and partially depleted CCDs,” Proc. 4th ESO Workshop on Optical Detectors for Astronomy, Garching, Germany (Kluwer, 2000).
[29] Karcher, A., et al., “Measurement of Lateral Charge Diffusion in Thick, Fully Depleted, Back-illuminated CCDs,” IEEE Trans. Nucl. Sci. 51 (2004).
[30] Fairfield, J., et al., “Reduced Charge Diffusion in Thick, Fully-Depleted CCDs with Enhanced Red Sensitivity,” IEEE Trans Nucl. Sci., 53 (2006).
[31] Tindall, C., et al., “Silicon Detectors for Low Energy Particle Detection”, IEEE Trans. Nucl. Sci. 55 (2008).
[32] Tarle, G., et al., “SNAP NIR Detectors,” Proc. SPIE 4850, 919 (2003).
[33] Brown, M., et al., “Development of NIR detectors and science-driven requirements for SNAP,” Proc. SPIE 6265, 626535 (2006).
[34] Smith, R., et al., “Noise and zero point drift in 1.7 μm cutoff detectors for SNAP,” Proc. SPIE 6276, 62760R (2006).
[35] Karcher, A., et al., “Integrating Signal Processing and A/D Conversion in One Focal-Plane Mounted ASIC, Turning photons into bits in the cold,” Scientific Detectors for Astronomy 2005, J. E. Beletic, J. W. Beletic, P. Amico editors, Springer (2006).
[36] Walder, J.P., et al., “A low power, wide dynamic range multi-gain signal processor for the SNAP CCD,” Nuclear Science Symposium Conference Record, 2003 IEEE (2003).
[37] Karcher, A., et al., “A Low Noise, Radiation Tolerant CCD Readout Processor for the Proposed SNAP Satellite,” IEEE Nuclear Science Symposium Conference Record, vol.2, pp.1069-1072 (2007).
[38] Krieger, B., et al., “A precision voltage and current reference for the SNAP CCD readout IC,” IEEE Trans. Nucl. Sci. (2007).
[39] Walder, J.P., et al., "A CCD clock controller ASIC using novel design techniques integrated in a CMOS 0.8μm SOI high voltage process," IEEE Nuclear Science Symposium Conference Record, vol.3, no., pp.2404-2407 (2007).
[40] Atwood, W., et al., "The Large Area Telescope on the Fermi Gamma-Ray Space Telescope Mission", ApJ, Vol 697, Issue 2, pp. 1071-1102 (2009).
[41] Mankins, J., "Technology Readiness Levels," White Paper, NASA Office of Space Access and Technology, April 6, 1995.
[42] Janesick, J., “Photon Transfer”, SPIE Press Book, Vol. PM170, 2007.
[43] Dawson, K., et al., "Radiation Tolerance of Fully-Depleted p-Channel CCDs Designed for the SNAP Satellite," IEEE Trans. Nucl. Sci. **55**, 1725-1735 (2008).
[44] Rhodes, J., et al., "The effects of charge transfer inefficiency on galaxy shape measurements," PASP Vol. 122, No. 890 (April 2010), pp. 439-450.
[45] Abiad, R., and Karcher, A., private communication.
[46] Loose, M., et al., "The SIDECAR ASIC — Focal Plane Electronics on a Single Chip", Proc. SPIE, 5904, 59040V (2005).
[47] Rauscher, B., et al., "Detectors for the James Webb Space Telescope Near-Infrared Spectrograph. I. Readout Mode, Noise Model, and Calibration Considerations", PASP, 119, No. 857, 768-786 (2007).
[48] Edelstein, J., et al., “Cryogenic Focal Plane Flatness Measurement with Optical Zone Slope Tracking,” Proc. SPIE, 8155A, 8155A22 (2011).